

A preconditioned solver for sharp resolution of multiphase flows at all Mach numbers

Pooria Hadikhani^a, Sahand Majidi^b and Asghar Afshari^{a,*}

^a School of Mechanical Engineering, College of Engineering University of Tehran, Tehran, Iran

^b Faculty of Mechanical and Energy Engineering, Shahid Beheshti University, A.C., Tehran, Iran

ARTICLE INFO

Article history:

Received: 15 March 2018

Accepted: 22 August 2018

Keywords:

Interface capturing

Multi-phase flows

Preconditioning

Five-equation model

Interface sharpening

ABSTRACT

A preconditioned five-equation two-phase model coupled with an interface sharpening technique is introduced for simulation of a wide range of multiphase flows with both high and low Mach regimes. Harten-Lax-van Leer-Contact (HLLC) Riemann solver is implemented for solving the discretized equations while tangent of hyperbola for interface capturing (THINC) interface sharpening method is applied to reduce the excessive diffusion of the method at the interface. In this work, preconditioning technique is used in a system of equations including viscous and capillary effects. Several one- and two-dimensional test cases are used to evaluate the performance and accuracy of this method. Numerical results demonstrate the efficiency of preconditioning in low Mach number flows. Comparisons between results of preconditioned and conventional system highlight the necessity of using preconditioning technique to reproduce main characteristics of low-speed flow regimes. Additionally, preconditioned systems transform to the conventional systems at high Mach number flows thus exhibiting the same level of accuracy as the standard flow solver. Therefore, the preconditioned compressible two-phase method can be used as an all-speed two-phase flow solver accounting for capillary and viscous stresses.

1. Introduction

Compressible two-phase flows have been an attractive field of research due to their many practical applications including fuel injection in internal combustion engines, jet atomization, pump cavitation and etc. [1, 2]. Various mathematical models, developed to describe the flow behaviour and interface topology in multiphase context, are divided into Eulerian-Eulerian (EE) and Lagrangian-Eulerian (LE) methodologies [3, 4]. In the LE description, a Lagrangian frame is used to represent the dispersed phase while a Eulerian frame is utilized for indicating the continuous phase [5]. In the EE description, both phases are represented in the Eulerian frame, therefore, the interface is clearly distinguished [6].

Diffuse interface method (DIM) [7] and sharp interface method (SIM) [8] are two main approaches in the numerical simulation of two-phase flows in the EE framework. SIM reconstructs interfaces and keeps discontinuities sharp by tracking them. On the other hand, DIM does not track the discontinuities and allows numerical diffusion at interfaces [9].

In DIM, the set of governing equations is derived via implementing the ensemble averaging procedure to the equations

of motion of the phases [10]. The resulting equations assume distinct velocities and pressures for each phase after averaging procedures and can take different forms [11-14]. This model has seven equations in one-dimensional flow and is numerically complex to solve [15]. This set of equations has been reduced using an asymptotic analysis and expressed in a homogenous model with single pressure and velocity. In this case, the reduced model has five equation in one-dimensional flow [16, 17]. The Reduced model describes the interface as a diffuse layer where the transition of physical quantities from one phase to another is smooth. Different numerical techniques have been introduced to reduce this numerical diffusion in the interface [18-21].

Modeling two-phase flow problems are encountered in a large number of situations ranging from high Mach number to low Mach number and incompressible flows. In compressible flows, low and high Mach number regimes exist simultaneously. Low Mach simulations with compressible approach have difficulties such as convergence rate and precision. Low Mach number flows typically have high convective to acoustic time scale ratios resulting into convergence difficulties [22, 23]. Moreover, the numerical solution of compressible equations does not converge to the incompressible solution [24]. To solve this difficulty, incompressible methods can be used in some cases. However, in

* Corresponding author. Tel.: +98-21-8208-9925; fax: +98-21-8801-3029; e-mail: afsharia@ut.ac.ir

the case of compressible multiphase flows where low and high Mach number regimes coexist, incompressible methods cannot be employed [25]. An effective technique to improve the convergence rate in low Mach number multiphase flows is the time-derivative preconditioning method originally developed by LeMartelot, Nkonga, Saurel [26]. This method is beneficial to retain the hyperbolic/parabolic properties of the compressible system in the low Mach number limit [27] and thus remedy the above mentioned challenges in compressible multiphase solvers.

More specifically, preconditioning methodology is used to modify the system eigenvalues to decrease the imbalance between eigenvalues in the low Mach number limit of compressible multiphase flows [25]. Turkel [27] used pseudo-compressibility approach to modify the incompressible inviscid equations to expedite the convergence in the steady state simulations. Turkel extended incompressible results to compressible low Mach number flows. Li, Gu [28] modified the wave speeds in Harten-Lax-van Leer (HLL) scheme to precondition the one phase Euler equations. Luo, Baum, Lohner [22] deployed time-derivative preconditioning along with the HLLC scheme to achieve an all speed flow solver for one phase compressible Euler equations. Murrone, Guillard [29] extended the one phase preconditioning method to solve the non-conservative two-phase Euler equations. LeMartelot, Nkonga, Saurel [26] applied Turkel's preconditioning

method to Godunov scheme for the solution of inviscid two-phase flows.

The main objective of this research is to develop a general flow solver that can simulate a wide range of regimes. To solve five-equation model, HLLC approximate Riemann solver [30] is applied. The HLLC solver is an extension to the HLL solver [31], whereby the contact discontinuity is restored. Capillary, viscous stress and gravitational forces are added in order to extend the generality of the flow solver. To overcome the high diffusivity of the diffuse interface methodology, an interface sharpening scheme could be used. In this research THINC interface sharpening of Shyue, Xiao [32] applied to the flow solver, because of its efficiency and simplicity. Preconditioning method of Turkel [27] is utilized to remove the limitation of compressible approach at low Mach speeds. This enables the flow solver to retain the incompressible solution in case of multiphase flows with Mach speeds tending to zero.

2. Formulation

Compressible five-equation model with capillary, viscous effect and gravity can be expressed in vector form as [16],

$$U_t + F_x + G_y = S \quad (1)$$

where

$$U = \begin{bmatrix} \rho_1 \alpha_1 \\ \rho_2 \alpha_2 \\ \rho u \\ \rho v \\ \rho E \end{bmatrix}, F = \begin{bmatrix} \alpha_1 \rho_1 u \\ \alpha_2 \rho_2 u \\ \rho u^2 + P \\ \rho uv \\ u(\rho E + P) \end{bmatrix}, G = \begin{bmatrix} \alpha_1 \rho_1 v \\ \alpha_2 \rho_2 v \\ \rho uv \\ \rho v^2 + P \\ v(\rho E + P) \end{bmatrix}, \quad (2)$$

$$S = \begin{bmatrix} 0 \\ 0 \\ \frac{\partial \tau_{xx}}{\partial x} + \frac{\partial \tau_{xy}}{\partial y} - \sigma \kappa \frac{\partial \alpha_1}{\partial x} + \rho g_x \\ \frac{\partial \tau_{xy}}{\partial x} + \frac{\partial \tau_{yy}}{\partial y} - \sigma \kappa \frac{\partial \alpha_1}{\partial y} + \rho g_y \\ \frac{\partial (u\tau_{xx} + v\tau_{xy})}{\partial x} + \frac{\partial (u\tau_{xy} + v\tau_{yy})}{\partial y} - \sigma \kappa \left(u \frac{\partial \alpha_1}{\partial x} + v \frac{\partial \alpha_1}{\partial y} \right) + \rho (u g_x + v g_y) \end{bmatrix}.$$

To represent the transition between the mediums, a phase indicator function (α_k) is introduced. The phase function is calculated from advection equation. In Eq. (2), α_k is the volume fraction defined as the ratio of the volume occupied by phase k over the total cell volume. To calculate volume fraction, the volume of fluid method is used where the solution of following equation is needed [33].

$$\frac{\partial \alpha_1}{\partial t} + u \frac{\partial \alpha_1}{\partial x} + v \frac{\partial \alpha_1}{\partial y} = 0 \quad (3)$$

This equation gives the volume fraction of the first phase and it is calculated in conjunction with Eq. (1). The volume fraction of the second phase can be obtained from the following equation:

$$\alpha_1 + \alpha_2 = 1 \quad (4)$$

The density, pressure and total specific energy are represented by ρ, P and E , u and v represent the components of the velocity. Mixture variables are defined as

$$\begin{aligned} \rho &= \sum_i \rho_i \alpha_i \\ \rho \vec{u} &= \sum_i \rho_i \alpha_i \vec{u} \\ \rho E &= \sum_i \alpha_i \rho_i E_i. \end{aligned} \quad (5)$$

Components of stress tensor in Eq. (2) are defined as

$$\begin{aligned} \tau_{xy} &= \mu \left(\frac{\partial v}{\partial x} + \frac{\partial u}{\partial y} \right) \\ \tau_{yy} &= 2\mu \frac{\partial v}{\partial y} - \frac{2}{3}\mu \left(\frac{\partial u}{\partial x} + \frac{\partial v}{\partial y} \right) \\ \tau_{xx} &= 2\mu \frac{\partial u}{\partial x} - \frac{2}{3}\mu \left(\frac{\partial u}{\partial x} + \frac{\partial v}{\partial y} \right). \end{aligned} \quad (6)$$

Liquids are considered incompressible in low pressures, while under very high pressures, it can be assumed as compressible material. Stiffened equation of state can be used to simulate this behavior of liquids [13]. This EOS takes the following form [34]

$$P_k = (\gamma_k - 1)\rho_k e_k - \gamma_k P_{\infty k} \quad (7)$$

where P_k , ρ_k and e_k are the pressure, density and specific internal energy of phase k , respectively. γ and P_{∞} are constants that depend on the phase under consideration. For perfect gases, γ is the ratio of specific heats and $P_{\infty} = 0$, so that the ideal gas relation is achieved. P_{∞} represents the molecular attraction between material molecules. For the large values of P_{∞} , stiffened equation of state describes the near-incompressible behavior of the material [35]. Considering stiffened equation of state, speed of sound is calculated by following equation

$$a = \sqrt{\frac{\gamma(P+P_{\infty})}{\rho}}. \quad (8)$$

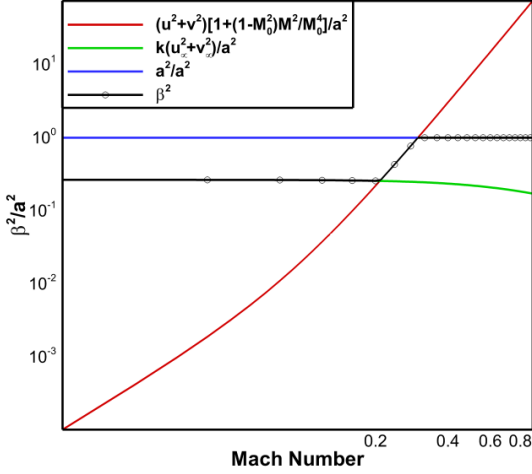


Figure 1. β^2/a^2 versus the Mach number.

By using the definition of mixture internal energy and Eq. (7), we have following expression for the mixture internal energy

$$\rho e = \sum_i \alpha_i \frac{P + \gamma_i P_{\infty i}}{\gamma_i - 1}. \quad (9)$$

The isobaric closure is implemented that leads to $P_1 = P_2 = P$ assuming that the artificial equation of state for the mixture takes same form as Eq. (7). According to Eq. (9), the equation of state parameters γ and P_{∞} are given as

$$\frac{1}{\gamma - 1} = \sum_i \frac{\alpha_i}{\gamma_i - 1}; \quad \gamma P_{\infty} = \frac{\sum_i \alpha_i \gamma_i P_{\infty i}}{\sum_i \frac{\alpha_i}{\gamma_i - 1}}. \quad (10)$$

3. Numerical Method

To solve Eq. (1) HLLC Riemann solver proposed by Toro [30] is used. The explicit formula of the Eq. (1) is

$$U_i^{n+1} = U_i^n + \frac{\Delta x}{\Delta t} \left[F_{i-\frac{1}{2}} - F_{i+\frac{1}{2}} \right] + \frac{\Delta y}{\Delta t} \left[G_{i-\frac{1}{2}} - G_{i+\frac{1}{2}} \right]. \quad (11)$$

HLLC numerical flux is defined as

$$F_{i+\frac{1}{2}}^{hllc} = \begin{cases} F_L & , \text{if } 0 \leq S_L \\ F_{*L} & , \text{if } S_L \leq 0 \leq S_* \\ F_{*R} & , \text{if } S_* \leq 0 \leq S_R \\ F_R & , \text{if } 0 \geq S_R \end{cases} \quad (12)$$

where S_L and S_R are the eigenvalues of the Jacobian matrix $(\partial F / \partial U)$ and are equal to:

$$\begin{cases} S_L = u - a \\ S_R = u + a \end{cases} \quad (13)$$

MUSCL scheme is used to construct the right and left side states of the Riemann problem at cell edges in the entire domain [36]. S_* is intermediate speed, calculated as below

$$S_* = \frac{P_R - P_L + \rho_L u_L (S_L - u_L) - \rho_R u_R (S_R - u_R)}{\rho_L (S_L - u_L) - \rho_R (S_R - u_R)}. \quad (14)$$

Intermediate flux vector is given as

$$F_{*K} = \frac{S_* (S_K U_K - F_K) + S_K (P_K + \rho_K (S_K - u_K) (S_* - u_K)) D_*}{S_K - S_*} \quad (15)$$

where

$$D_* = [0 \quad 0 \quad 1 \quad 0 \quad S_*]^T. \quad (16)$$

To reduce the numerical diffusion and capture a sharp interface, THINC scheme of Shyue, Xiao [32] is implemented before the solution of Riemann problems at cell edges are obtained. This scheme modifies the input states of the Riemann problems at cell edges in the vicinity of the interface, previously calculated using MUSCL scheme. First, the computational cells located near the interface are identified as those satisfying the following condition

$$(\alpha_{i+1} - \alpha_i)(\alpha_i - \alpha_{i-1}) > 0. \quad (17)$$

Afterwards, volume fraction is computed based on the following hyperbolic function

$$\alpha_i(x) = \frac{1}{2} \left[1 + \sigma_i \tanh \left(\delta \left(\frac{x - x_{i-1/2}}{\Delta x_i} - \bar{x}_i \right) \right) \right]. \quad (18)$$

In Eq. (18) σ represents the sign of volume fraction change within interface cells and δ is a free parameter that controls the thickness of the jump. \bar{x} can be specified by conservation of volume fraction assumption.

$$\bar{x} = \frac{1}{2\delta} \ln \left[- \frac{e^{\delta(2+\frac{1}{\sigma})} - e^{\delta(1+\frac{2\alpha_i}{\sigma})}}{e^{\delta} - e^{\delta(1+\frac{2\alpha_i}{\sigma})}} \right] \quad (19)$$

Using new volume fraction distribution, variables at interface are modified before solving the Riemann problem.

To consider capillary effects, the continuum surface force (CSF) model of Brackbill, Kothe, Zemach [37] is utilized where volume fraction is used as color function. Surface curvature [38] is calculated by

$$\kappa = -(\nabla \cdot \hat{n}) \quad (20)$$

where \hat{n} is the unit normal to the surface, which is computed by

$$\hat{n} = \frac{\nabla \alpha}{|\nabla \alpha|}. \quad (21)$$

4. Preconditioning Method

Non-conservative form of equations is used to develop the preconditioning method, then the preconditioned equations are transformed into conservative form. Considering $(\alpha_1, \rho_1, \alpha_2, \rho_2, u, v, P)$ as primitive variables the non-conservative form of Eq. (1) is

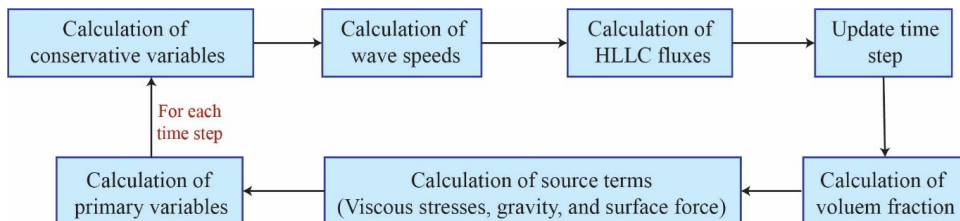


Figure 2. Flowchart of the solution procedure.

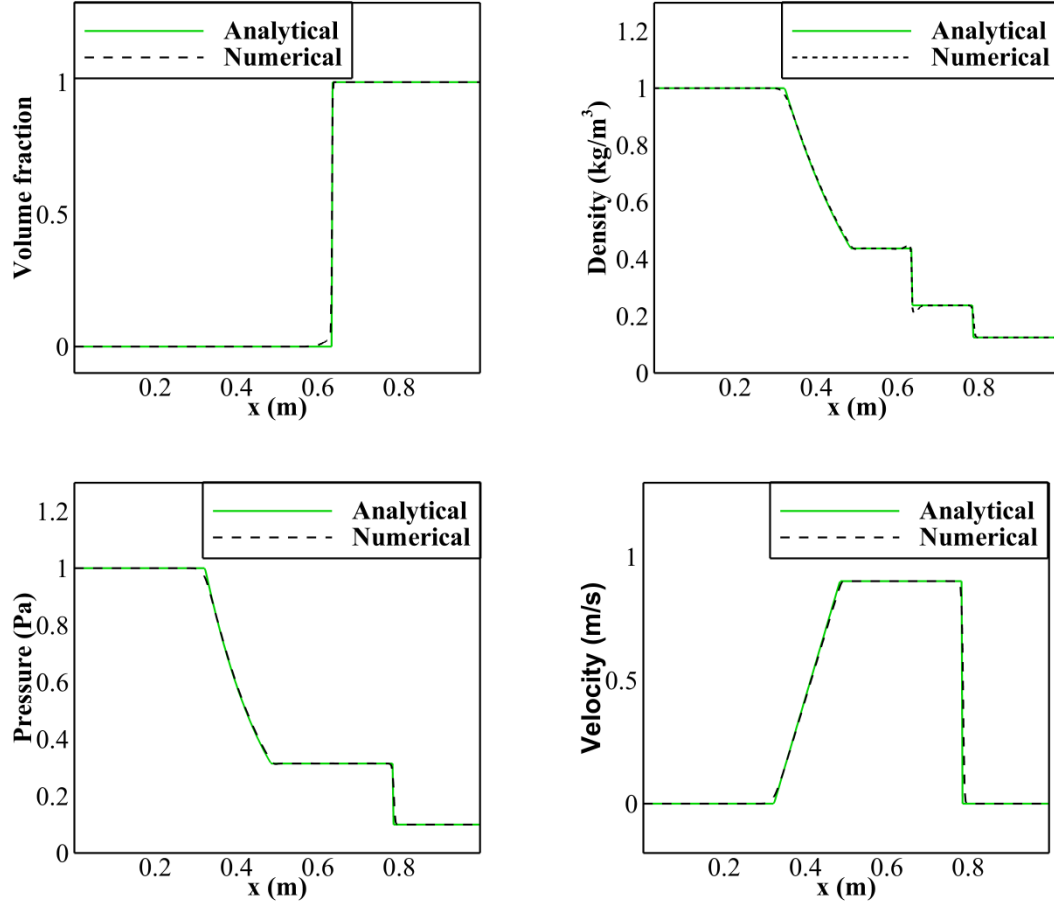


Figure 3. Air-helium shock tube problem at $t=0.15s$, solid lines indicate exact solution while dashed lines indicate the numerical solution.

$$\frac{\partial w}{\partial t} + A \frac{\partial w}{\partial x} + B \frac{\partial w}{\partial y} = H. \quad (22)$$

where

$$W = \begin{bmatrix} P \\ \alpha_1 \rho_1 \\ \alpha_2 \rho_2 \\ u \\ v \end{bmatrix}, \quad A = \begin{bmatrix} u & 0 & 0 & \rho a^2 & 0 \\ 0 & u & 0 & \alpha_1 \rho_1 & 0 \\ 0 & 0 & u & \alpha_2 \rho_2 & 0 \\ \frac{1}{\rho} & 0 & 0 & u & 0 \\ 0 & 0 & 0 & 0 & u \end{bmatrix}, \quad (23)$$

$$B = \begin{bmatrix} v & 0 & 0 & 0 & \rho a^2 \\ 0 & v & 0 & 0 & \alpha_1 \rho_1 \\ 0 & 0 & v & 0 & \alpha_2 \rho_2 \\ 0 & 0 & 0 & v & 0 \\ \frac{1}{\rho} & 0 & 0 & 0 & v \end{bmatrix},$$

$$H = \begin{bmatrix} 0 \\ 0 \\ 0 \\ \frac{1}{\rho} \left(\frac{\partial \tau_{xx}}{\partial x} + \frac{\partial \tau_{xy}}{\partial y} - \sigma \kappa \frac{\partial \alpha_1}{\partial x} \right) + g_x \\ \frac{1}{\rho} \left(\frac{\partial \tau_{xy}}{\partial x} + \frac{\partial \tau_{yy}}{\partial y} - \sigma \kappa \frac{\partial \alpha_1}{\partial y} \right) + g_y \end{bmatrix}.$$

Eq. (22) is preconditioned as follows

$$P_p \frac{\partial w}{\partial t} + A \frac{\partial w}{\partial x} + B \frac{\partial w}{\partial y} = H \quad (24)$$

where

$$P_p = \begin{bmatrix} \frac{a^2}{\beta^2} & 0 & 0 & 0 & 0 \\ 0 & 1 & 0 & 0 & 0 \\ 0 & 0 & 1 & 0 & 0 \\ 0 & 0 & 0 & 1 & 0 \\ 0 & 0 & 0 & 0 & 1 \end{bmatrix}. \quad (25)$$

In the preconditioner matrix, a is the speed of sound and parameter β^2 is proportional to the local speed ($u^2 + v^2$). As the Mach number tends to zero, a^2/β^2 tends to infinity. In this case, the time derivative of pressure must be zero in order for the pressure equation to remain finite. Under the condition of zero pressure time derivative, the system tends to incompressible equation. However, this procedure has difficulties in stagnation points. To overcome this problem a cutoff is introduced by Turkel, Vasta, Radespiel [25]. Therefore β^2 is calculated using following equation

$$\beta^2 = \min \left(\max \left((u^2 + v^2) \left(1 + \frac{1-M_0^2}{M_0^4} M^2 \right), K(u_\infty^2 + v_\infty^2) \right), a^2 \right). \quad (26)$$

where K is a constant between 0.4 and 1, u_∞ , and v_∞ are freestream velocity components and M_0 is the Mach number which determines the switch-off threshold of the preconditioning technique, in this case, β^2 is equal to a^2 . In Figure 1, the behavior of Eq. (26) is presented.

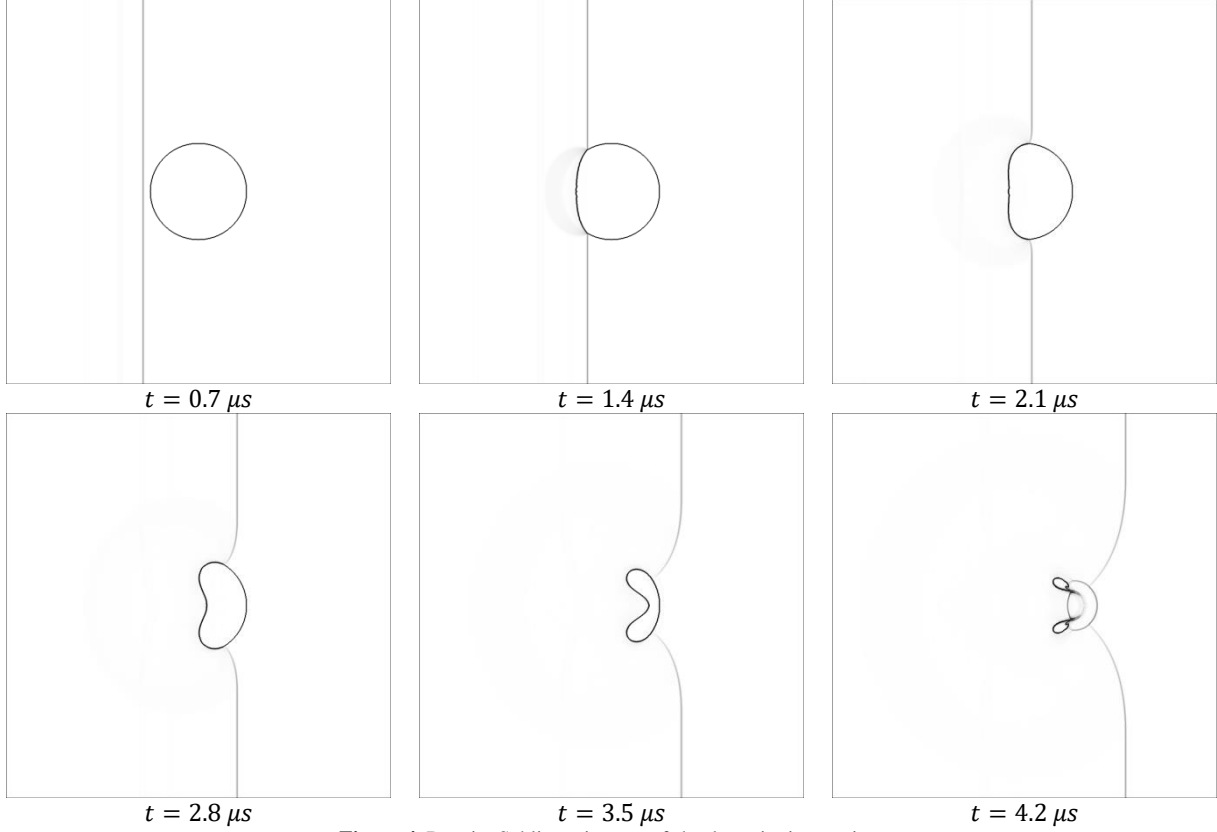


Figure 4. Density Schlieren images of shock-cavity interaction.

Using Eq. (24), the eigenvalues of preconditioned system in the x-direction are

$$S_L = \frac{\left(1 + \frac{\beta_L^2}{a_L^2}\right)u_L - \sqrt{\left(1 - \frac{\beta_L^2}{a_L^2}\right)^2 u_L^2 + 4\beta_L^2}}{2} \quad (27)$$

$$S_R = \frac{\left(1 + \frac{\beta_R^2}{a_R^2}\right)u_R + \sqrt{\left(1 - \frac{\beta_R^2}{a_R^2}\right)^2 u_R^2 + 4\beta_R^2}}{2}.$$

As can be seen, preconditioned eigenvalues approach the non-preconditioned values when β^2/a^2 tends to unity. Therefore,

$$P_c = \begin{bmatrix} 1 & 0 & 0 & 0 & 0 \\ 0 & 1 & 0 & 0 & 0 \\ 0 & 0 & 1 & 0 & 0 \\ 0 & 0 & 0 & 1 & 0 \\ \left(\frac{\beta^2}{a^2} - 1\right)\frac{(u^2+v^2)}{2} & \left(\frac{\beta^2}{a^2} - 1\right)\frac{(u^2+v^2)}{2} & u\left(1 - \frac{\beta^2}{a^2}\right) & v\left(1 - \frac{\beta^2}{a^2}\right) & \frac{\beta^2}{a^2} \end{bmatrix}. \quad (29)$$

Figure 2 demonstrates the flowchart of the solution procedure. Initially, the conservative variables are computed using Eq. (2). Then the flow solver calculates the wave speeds and HLLC fluxes by using Eq. (27) and (12) respectively. Eq. (27) is the preconditioning alternative of the standard equation Eq. (13) in the original HLLC method to calculate wave speeds. Then, the vector of conservative variables is updated at every computational cell in the entire domain. Next, the updated values of volume fraction and the source terms including viscous terms and surface tension are computed using Eq. (3) and Eq. (2). Finally, the new values of primary variables are obtained at the end of the time step.

preconditioned system is effective in areas with negligible local Mach numbers and switches back to the conventional system in high compressibility regions.

The conservative form of preconditioned equations is achieved by using Eq. (24)

$$P_c \frac{\partial U}{\partial t} + \frac{\partial F}{\partial x} + \frac{\partial G}{\partial y} = S \quad (28)$$

where

5. Numerical results

In this section, several test cases are used to evaluate the performance of the flow solver. The assessment begins with a one-dimensional two-phase flow test to compare the obtained numerical solutions with the exact ones. After that, the flow solver is used to simulate under-water explosion and shock cavity interaction in order to evaluate the performance of the flow solver when phases have a large difference of densities. The accurate modelling of the surface-tension, gravity and viscous stresses in the flow solver is investigated by simulating Rayleigh-Taylor instability. Next, the enhancement made in simulating low Mach-number flow regimes, due to the employment of the preconditioning method, is highlighted in the numerical study of

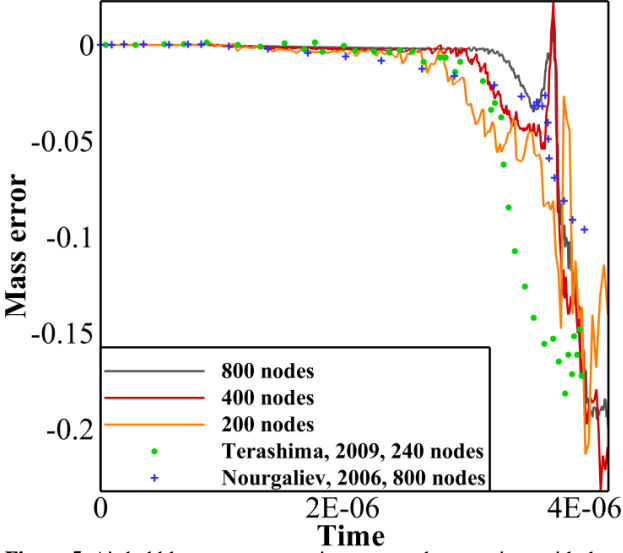


Figure 5. Air bubble mass conservation error and comparison with the results of Terashima, Tryggvason [39] and Nourgaliev, Dinh, Theofanous [40].

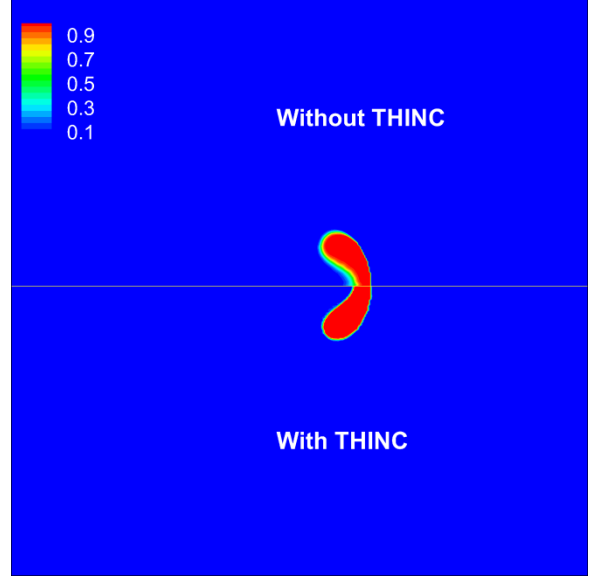


Figure 6. Comparison of interface of shock-cavity interaction at $t = 3.5 \mu s$.

the broken dam problem. In the end, the rising bubble test case is simulated by a preconditioned flow solver. In this case, the performance of the preconditioning method is compared with incompressible simulation.

5.1. Air-helium shock tube problem

Air-helium shock tube, that is studied by So, Hu, Adams [19], is investigated in this section. A shock tube with a length of 1m is used to appraise the ability of the method in capturing shocks in two-phase flows. The interface is located at $x = 0.5 m$ where the left side of the tube is filled with air with thermodynamic properties $(\gamma, P_\infty) = (1.4, 0)$ and the right side with helium with thermodynamic properties $(\gamma, P_\infty) = (1.667, 0)$. Air has initial state $(P, \rho, u) = (1.0, 1.0, 0)$ and helium has initial condition $(P, \rho, u) = (0.1, 0.125, 0)$. The simulation is done with 400 grid cells and results are presented at time 0.15 s. Results are shown in Figure 3 where the exact solution is exhibited for comparison. The exact solution is computed using the methodology provided by Toro [30]. As shown in Figure 3, the initial pressure discontinuity creates a right moving shock wave into the helium phase and left moving rarefaction wave to the air phase. This comparison shows the capability of the numerical method to predict the shock wave and the rarefaction wave. The numerical results are in good agreement with the exact solution.

In Table 1, L_1 error and also error order of flow solver with and without THINC interface sharpening are calculated for density at $t = 0.15 s$. L_1 errors are computed using the absolute difference between the numerical result and the corresponding exact solution

, both calculated using the same grid resolution. Comparison of the results shows that L_1 error is reduced by implementing the interface sharpening technique and the error order is increased when THINC method is applied.

Table 1. L_1 and orders of truncation error for air-helium shock tube problem

Grid resolution	Without THINC		With THINC	
	L_1 error	L_1 error order	L_1 error	L_1 error order
100	0.00913		0.00931	
200	0.00500	0.86873	0.00417	1.15675
400	0.00278	0.84893	0.00202	1.04983
800	0.00157	0.82077	0.00100	1.00622
1600	0.00087	0.84834	0.00050	0.99840

5.2. Shock cavity interaction

Shock cavity interaction test case is employed to verify the performance of the solver when there is a large density jump across the interface. As investigated by Terashima, Tryggvason [39] and Nourgaliev, Dinh, Theofanous [40] initially a cylindrical air bubble with diameter of 6 mm is placed in a water pool. The constant parameters for EOS are given in below

$$\gamma = 1.4, P_\infty = 0 \text{ for air}$$

$$\gamma = 4.4, P_\infty = 6 \times 10^8 \text{ for water}$$

The computational domain is a square of size $24 \times 24 mm^2$. The air bubble with a density of $1.2 kg/m^3$ is located at the center of the square surrounded by water with its density equal to $1000 kg/m^3$. The initial pressure of air bubble and pre-shocked

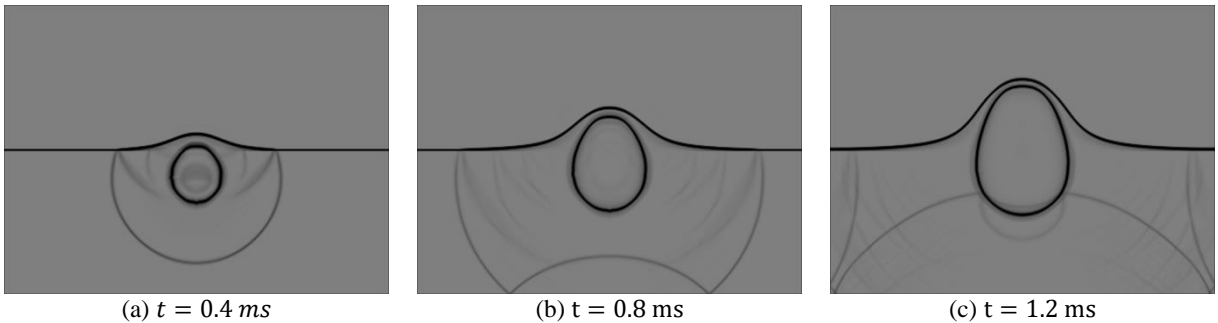


Figure 7. Density schlieren images of numerical simulation of under-water explosion.

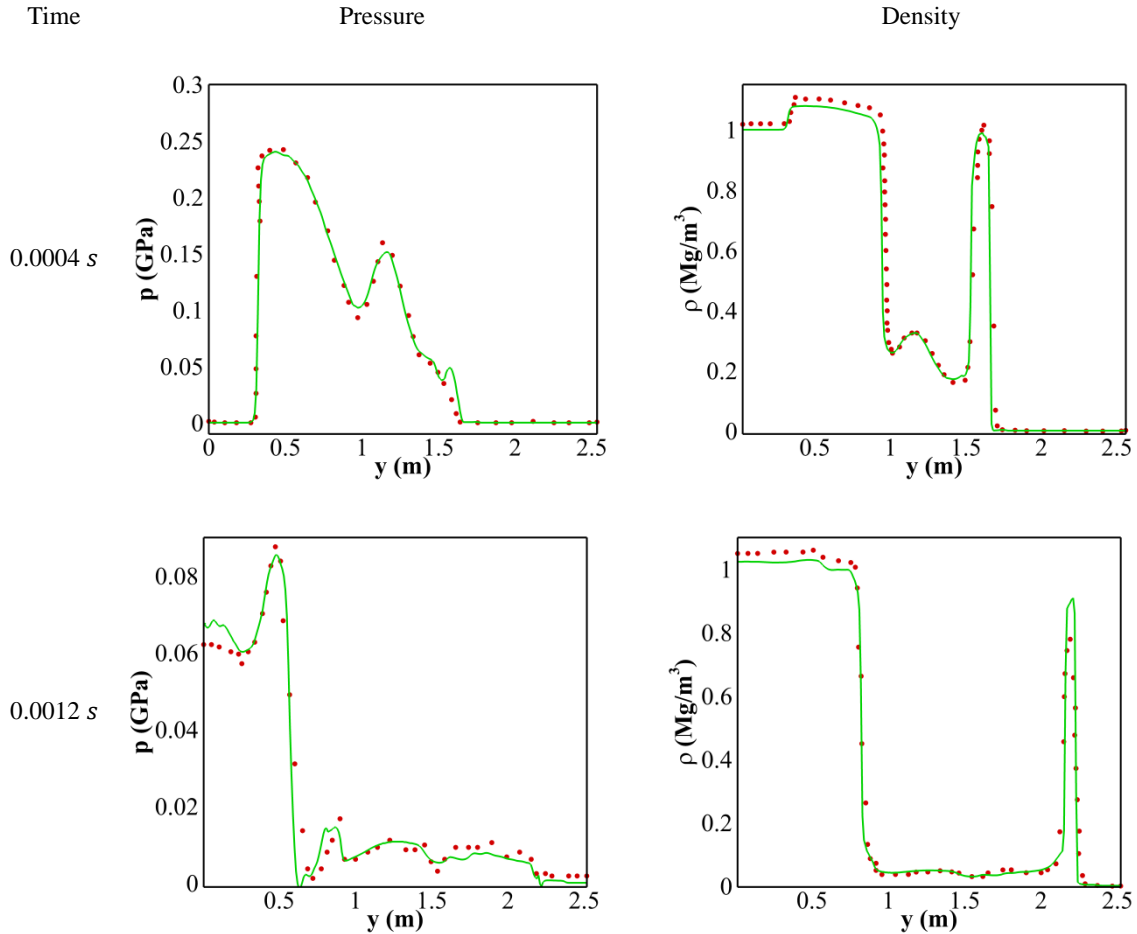


Figure 8. Density and pressure distribution of under-water explosion along vertical centerline. Solid lines are the results obtained using the DIM code and the dotted points are the results from Shyue [43] using interface capturing method.

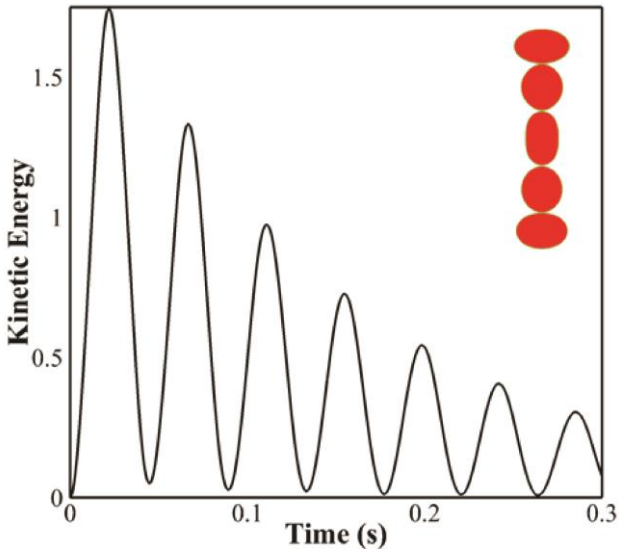


Figure 9. Changes of the kinetic energy of an oscillating drop vs. time.

water is set equal to $1 \times 10^5 Pa$. A right moving shock with the speed of $u = 681.58 m/s$ is located at $x = 6.6 mm$. Post-shock water density and pressure are $1323.65 kg/m^3$ and $1.9 \times 10^9 Pa$ respectively.

A 400×400 grid is used to simulate this test problem. Density schlieren images are presented in Figure 4. At $t = 1.4 \mu s$ shock wave collide the left side of the bubble and creates a shock wave inside the air region and reflecting rarefaction wave into the water

phase. Moreover, since the sound speeds in water and air are different, the shock front begins to twist. Subsequently, as the shock accelerates the bubble interface, it becomes involute and a liquid water jet is formed [41]. This jet moves along the centerline of the cylinder into the right. Eventually the bubble is separated into two lobes as the liquid jet drives through the bubble. The results are in good agreement with the previous simulations [39, 40]. The reported maximum water jet velocity when the shock wave hits the bubble by Nourgaliev, Dinh, Theofanous [40] is 2850 m/s and by Majidi, Afshari [42] is 2846 m/s. The maximum water jet velocity in our simulation is 2984 m/s. Furthermore, the results are in qualitative agreement with the experimental observations of Bourne, Field [41].

To gain a better insight into the performance of the solver, histories of air bubble mass conservation error is shown in Figure 5 along with the results from Terashima, Tryggvason [39] and Nourgaliev, Dinh, Theofanous [40]. Mass conservation errors are less than 0.5% before the breakup occurs at $t = 3.7 \mu s$, after that errors are grown very rapidly. Comparison of different grid resolutions (200×200 , 400×400 and 800×800) in Figure 5 indicates a decrease in mass conservation error when finer grids are utilized. By using the 800 grid resolution we can achieve a better mass conservation error than the results of Terashima, Tryggvason [39] and Nourgaliev, Dinh, Theofanous [40].

Figure 6, exhibits the effect of interface sharpening on the volume fraction of air bubble at $t = 3.5 \mu s$ for 400×400 grid. It is seen that THINC method is successful in reducing the thickness of the interface, thus improving the interface capturing quality.

5.3. Underwater explosion

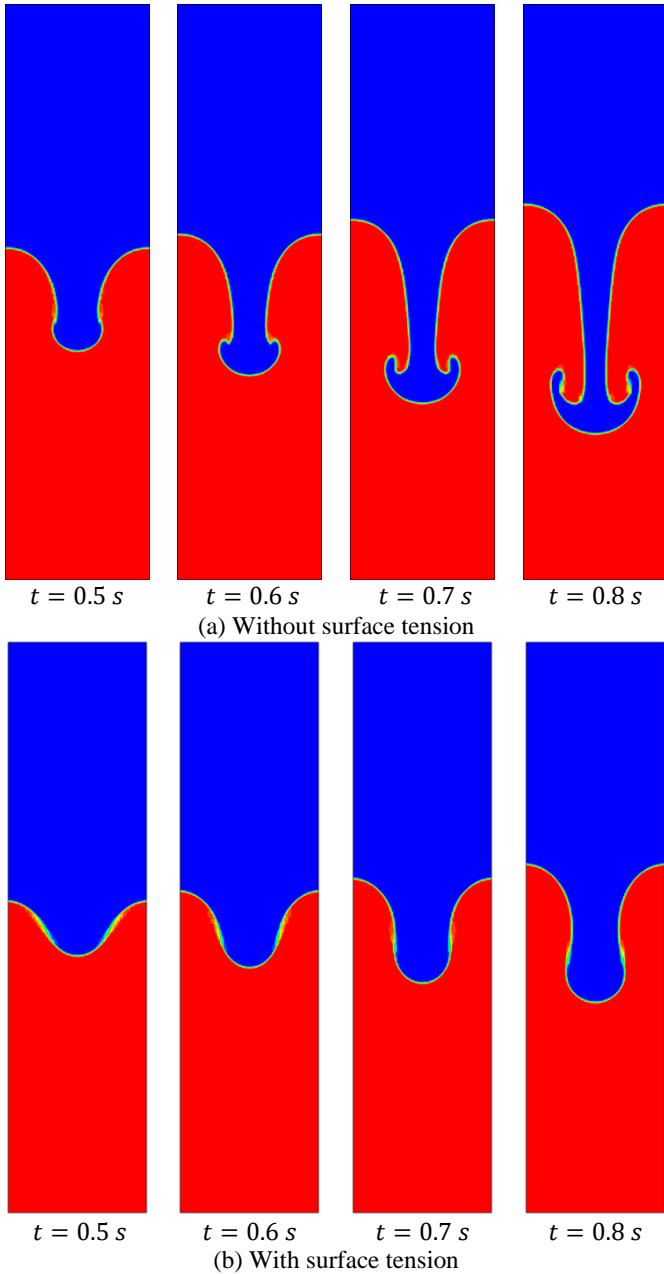


Figure 10. Volume fraction contours of Rayleigh-Taylor instability simulation.

Underwater explosion test has previously been simulated by Shyue [43] and Hu, Adams, Iaccarino [44]. Simulation is performed in a $[0,4] \times [0,3]$ rectangular domain and the interface of air and water is set at $y = 1.5 m$. The gaseous phase residing above the interface has the vector of properties $(P, \rho, \gamma, P_\infty) = (1.01325 \times 10^5 Pa, 1.225 kg/m^3, 1.4, 0)$. The fluid below the interface is water with the properties $(P, \rho, \gamma, P_\infty) = (1.01325 \times 10^5 Pa, 1000 kg/m^3, 4.4, 6 \times 10^8)$. Initially a circular bubble with a diameter of $0.24 m$ containing high pressure gas with a pressure of $1 \times 10^9 Pa$ and a density of $1250 kg/m^3$ is placed in the liquid phase with its center located at $(2, 1.2) m$. The simulation is carried out on a 400×300 uniform grid.

The schlieren images of density are presented in Figure 7. In the beginning of the simulation, high pressure of the air bubble creates outward shock wave and inward rarefaction wave. Outward shock wave is reflected as a rarefaction wave, after interacting with the air and water interface. Reflecting rarefaction

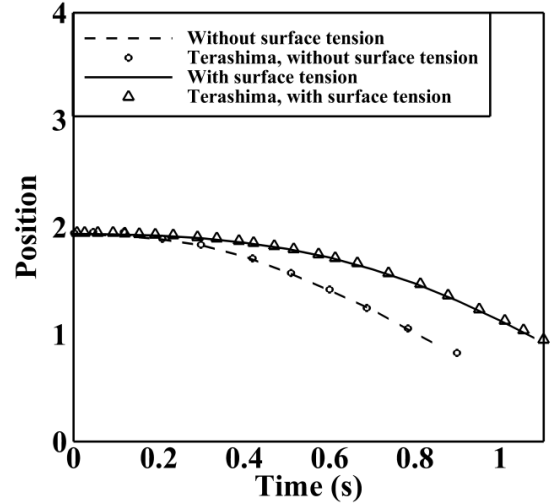


Figure 11. Spike front position in comparison with the results of Terashima, Tryggvason [39].

wave causes the bubble to transform into an oval like shape and accelerates it toward the interface [45]. Figure 8 presents the density and pressure distribution at $t = 0.4 ms$ and $t = 1.2 ms$ along the vertical centerline, and shows a qualitative agreement with the results presented by Shyue [43]. Pressure and density changes dramatically along $x = 2 m$ and Figure 8 shows that the numerical method can simulate the problems with high density and pressure ratios correctly.

5.4. Oscillating drop

The motion of deformed droplet arising from the surface tension is a suitable test case to evaluate the numerical tool in simulating these type of instabilities. In this section, simulation of the deformed droplet with the following initial shape is carried on:

$$\frac{(x-0.5)^2}{0.2^2} + \frac{(y-0.5)^2}{0.12^2} = 1. \quad (30)$$

The computational domain is a $1 m \times 1 m$ square with 40000 square grid cells. The surface tension between the two fluids is $\sigma = 342$. The physical properties of the air surrounding the water droplet are $(\gamma, P_\infty, \rho) = (1.4, 0, 1)$ and the properties of the water are $(\gamma, P_\infty, \rho) = (2.4, 10^7, 100)$. Figure 9 shows the changes in the kinetic energy of the water droplet over time. In the beginning, the droplet is at rest and its kinetic energy is zero. At this time, the interface starts to move because of surface forces. When the droplet reaches to the circular shape, most of the potential energies coming from surface tension converts to the kinetic energy. The droplet deformation continues. At this point most of the kinetic energy is retrieved in the form of interfacial potential energy. The droplet oscillation continues until the initial potential energy is totally dissipated due to viscous effects.

In this problem, the oscillation period achieved from the simulation is $T = 0.044885 s$. This value can be compared with the analytical value from the Rayleigh formula for two phase flows

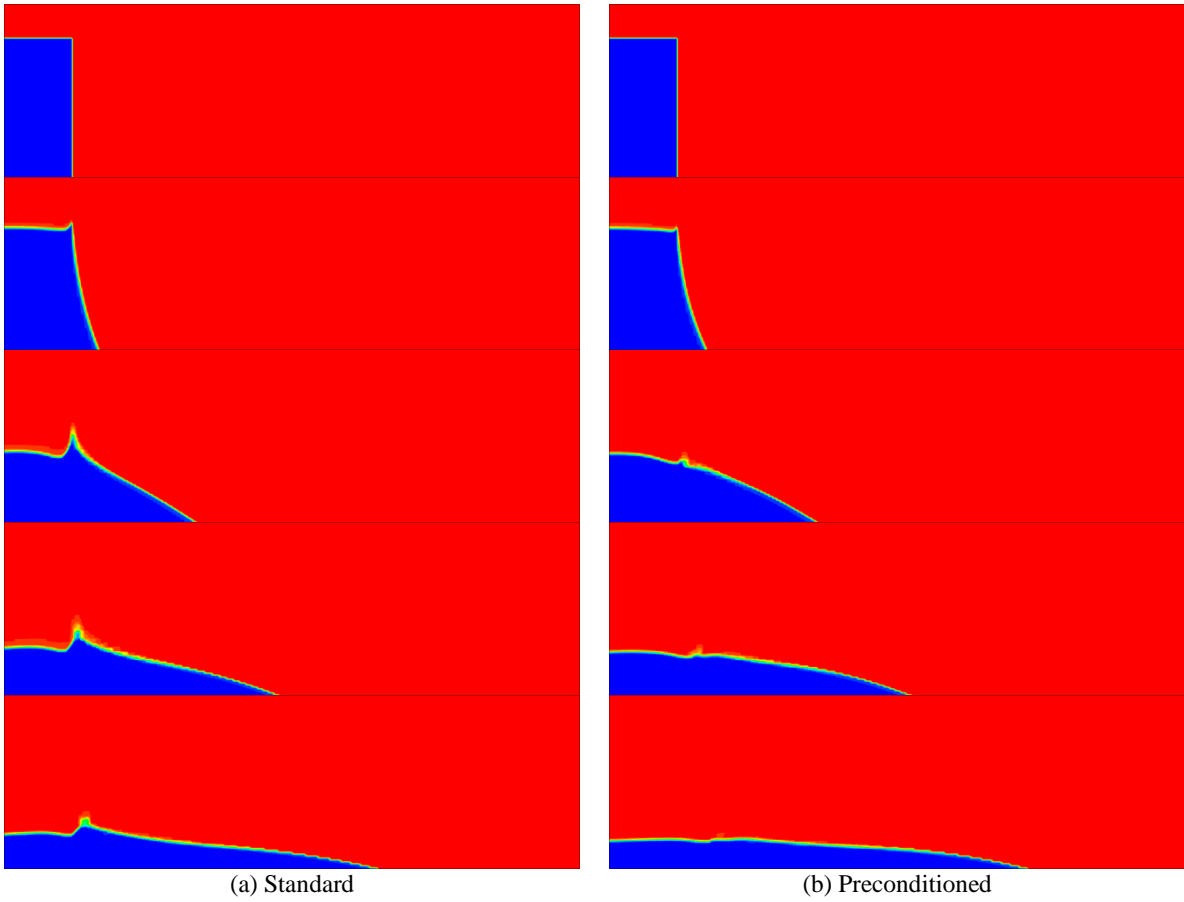


Figure 12. Broken dam simulation at five different times 0, 0.06 s, 0.15 s, 0.21 s and 0.281 s.

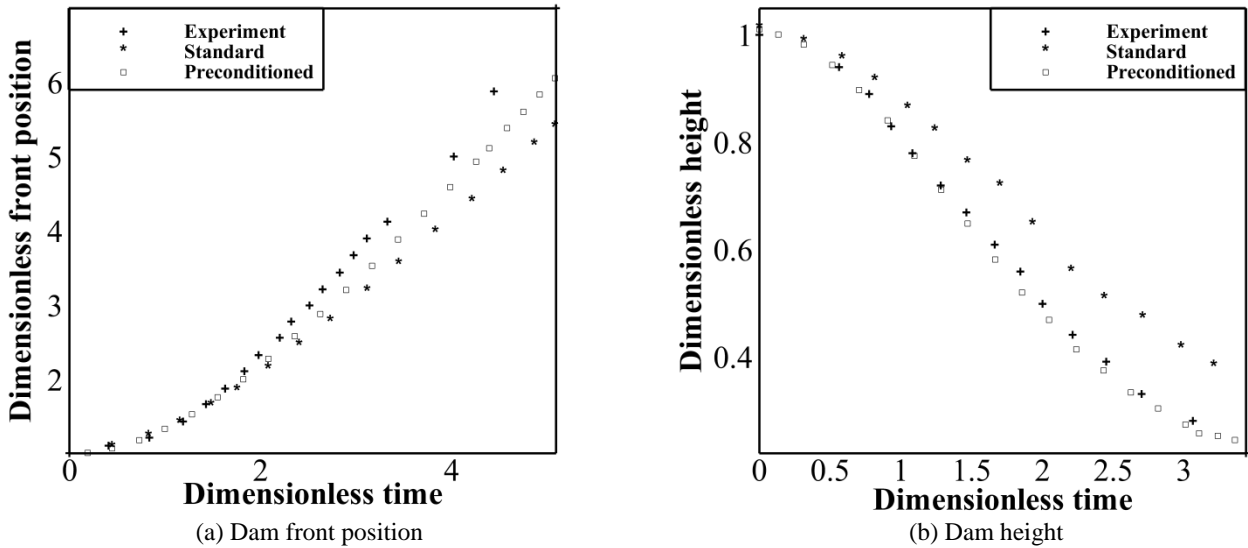


Figure 13. Comparison broken dam numerical results with experimental data [47].

[46]. The relation for droplet oscillation with density ρ_l with surrounding fluid of ρ_g density is as follows:

$$\omega^2 = (o^3 - o) \frac{\sigma}{(\rho_l + \rho_g)R^3}, T = \frac{2\pi}{\omega}. \quad (31)$$

In this equation, o is the vibrational mode and R is the radius of the droplet in equilibrium. The droplet in this simulation vibrates with the second vibrational mode and its radius at equilibrium is 0.15825 m. Thus, the analytical oscillation period is calculated as

$T = 0.0478889$ s, indicating a 6% difference with the numerically obtained value.

5.5. Rayleigh-Taylor instability

In this section the Rayleigh-Taylor instability is considered as an excellent test problem to evaluate the capability of our numerical solver to model gravitational forces, surface tension and

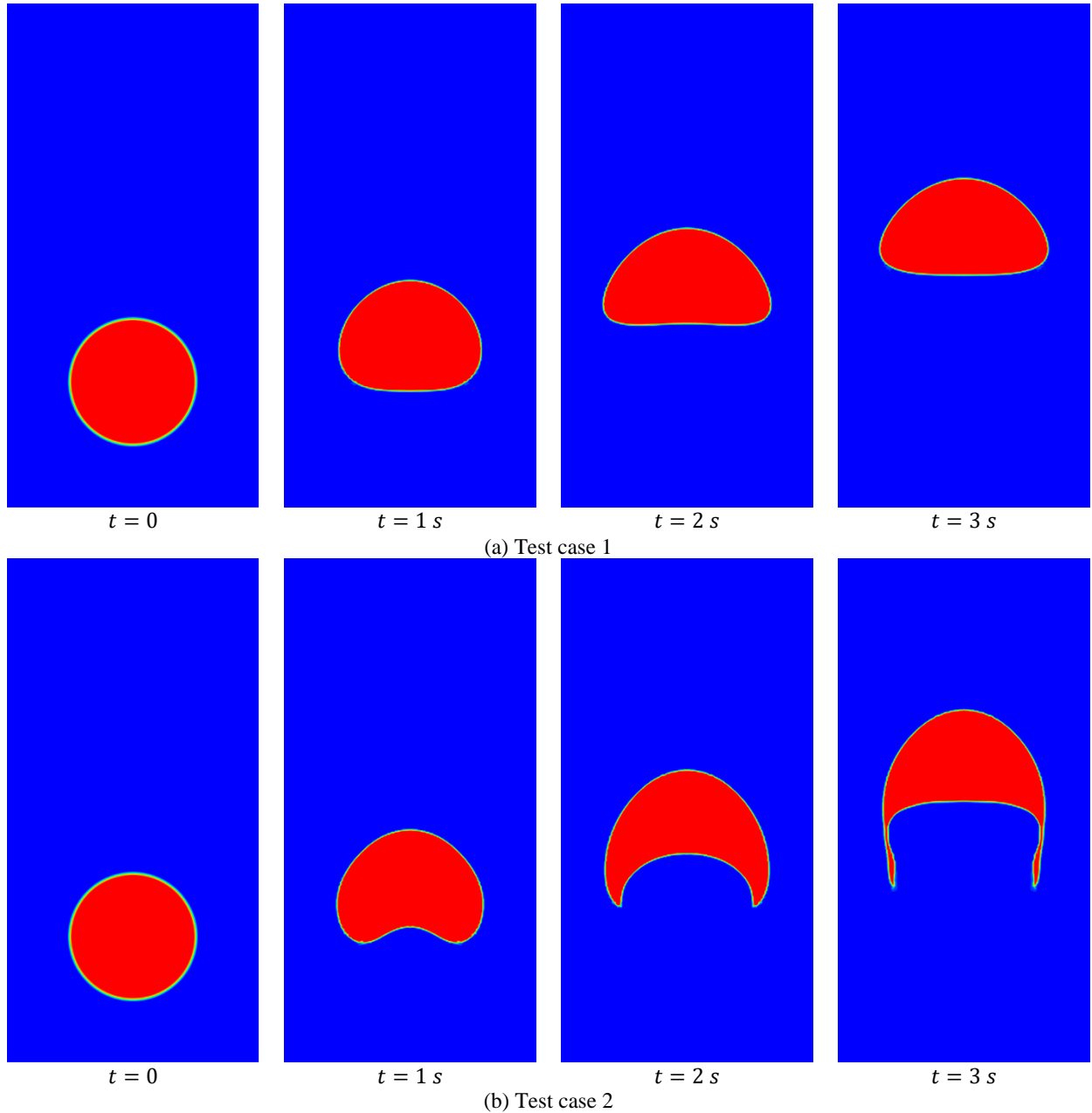


Figure 14. Time evolution of the bubble shape.

viscous stresses. This test is simulated by Terashima, Tryggvason [39]. The computational domain is a $1\text{m} \times 4\text{m}$ rectangle covered by a uniform grid of 50×200 computational cells. Initially, the upper part of the domain is occupied by a heavy fluid with density of 1.225 kg/m^3 and a light fluid with density of 0.1694 kg/m^3 is residing at the lower part. The viscosity for both fluids, surface tension and gravitational acceleration are set equal to $0.00313\text{ Pa}\cdot\text{s}$, 0.1531 N/m and 9.8 m/s^2 , respectively. Reflecting boundary condition is imposed on top and bottom edges of the domain and periodic boundary condition is employed at left and right boundaries.

Figure 10 shows the results for the simulation of the Rayleigh-Taylor instability with/without surface tension. Comparison of the spike front position obtained from the flow solver with the results of the Terashima, Tryggvason [39] is presented in Figure 11. A very good agreement is observed between our results and these obtained by Terashima, Tryggvason [39] which indicates the

ability of the flow solver in simulating problems with surface tension.

5.6. Broken dam

In this section broken dam test case experimentally studied by Martin, Moyce [47] is investigated. In this test, a stationary rectangular water column collapses due to the presence of gravity on a horizontal plane. This test was simulated by Murrone, Guillard [29] using a non-conservative preconditioned form of equations to simulate this problem.

In our simulation, a rectangular domain of size 0.5×0.15 is discretized using a 300×90 uniform grid. Initially a quiescent 0.06×0.12 water column with density and pressure of 1000 kg/m^3 and 101325 Pa is located at the lower left corner of the domain. The rest of the domain is occupied by air with density of 1.2 kg/m^3 and pressure of 101325 Pa . Stiffened equation of state is used for water with constant parameters of $(\gamma, P_\infty) = (4.4, 6 \times 10^8)$ and ideal gas equation of state is used for

5.7. Rising bubble

The last test problem considered in the present paper is rising bubble, previously studied by Hysing, Turek, Kuzmin, Parolini, Burman, Ganesan, Tobiska [49] to see the performance of the flow solver in simulation of low Mach number flows. The two main non-dimensional numbers for determination of flow regime are Reynolds number and Eötvös number.

$$Re = \frac{\rho_1 D \sqrt{gD}}{\mu_1}, Eo = \frac{\rho_1 g D^2}{\sigma} \quad (32)$$

In Eq. (32), the subscript 1 represents the denser fluid. In this test, a rectangular domain of size 1 m × 2 m is used where a circular bubble with diameter of $D = 0.5$ m is centered at [0.5 m, 0.5 m]. The physical parameters for the two test case considered in this section (Table 2), are similar to those given by Hysing, Turek, Kuzmin, Parolini, Burman, Ganesan, Tobiska [49].

Table 2. Initial states of the rising bubble simulation

Test case	ρ_1	ρ_2	μ_1	μ_2	Re	Eo
1	1000	100	10	1	35	10
2	1000	1	10	0.1	35	125

Figure 14, shows the time evolution of the bubble shape. The diagram of bubble shapes that is reported by Clift, Grace, Weber [50] can be used for qualitative comparison. For the test case 1, where the effects of surface tension is dominant, bubble begins to stretch horizontally. Due to surface tension, Bubble tends to maintain its circular shape and after a time it reaches an ellipsoidal shape as expected in the bubble shape diagram. In test case 2, decrease in surface tension causes the formation of the two sharp corners. Based on the Re and Eo of this test, the bubble shape diagram predicts the “skirted” regime for the bubble, that matches that of simulated results. As shown in Figure 15, the center of mass position of bubble is plotted versus time for both cases, compare reasonably well with the results obtained by Hysing, Turek, Kuzmin, Parolini, Burman, Ganesan, Tobiska [49] in incompressible framework. This indicates the successful treatment of viscous stress, surface tension and gravitational effects by our developed flow solver in low Mach number regimes. A qualitative comparison of shape of the bubble at time $t = 3$ s for results of standard, preconditioned and Hysing, Turek, Kuzmin, Parolini, Burman, Ganesan, Tobiska [49] is shown in Figure 16. The bubble shape predicted by the preconditioned method is seen to be more compatible with that obtained from the incompressible solution

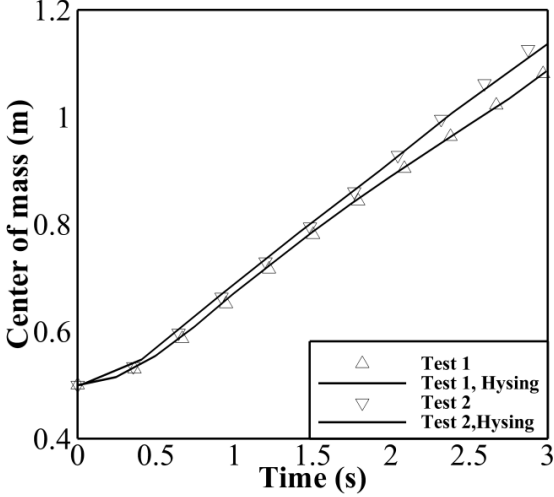


Figure 15. Comparison the position of center of mass of bubble with the results of Hysing, Turek, Kuzmin, Parolini, Burman, Ganesan, Tobiska [49].

air with specific heat ratio of $\gamma = 1.4$. Gravitational acceleration is set equal to 9.81 m/s^2 . Mach number in this simulation is very low; therefore the preconditioning is expected to increase the accuracy of the numerical results. To accentuate the impact of preconditioning, this problem is also simulated using the conventional compressible multiphase algorithm.

Standard and preconditioned broken dam simulation results are presented in Figure 12 at five different times 0, 0.06 s, 0.15 s, 0.21 s and 0.281 s. As it is evident from Figure 12, results of preconditioned and conventional solver are different, because of the difference in calculation of eigenvalues in these methods. To have a better comparison between these methods, in Figure 13 front position and height of the dam is indicated alongside the experimental data. As anticipated, preconditioning method leads to more accurate results compared to the conventional method. This is because pressure fluctuations predicted by conventional numerical methods are not consistent with their theoretical counterpart [48]. In Figure 13, time and front position are nondimensionalized by $time \times \sqrt{2g/a}$ and x/a in Figure 13(a), and by $time \times \sqrt{g/a}$ and $z/(2a)$ in Figure 13(b), where a is the initial width of water column.

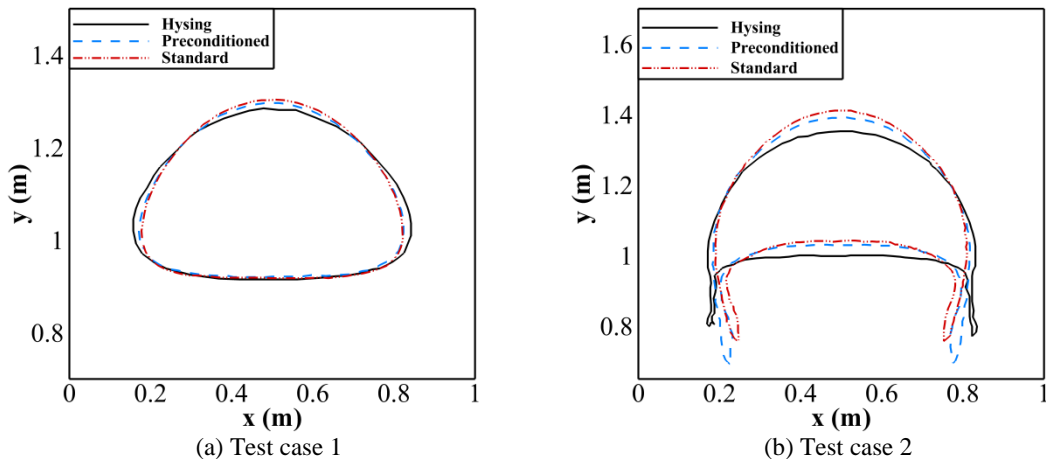


Figure 16. Comparison the simulated bubble shape by preconditioned and standard method with the results of Hysing, Turek, Kuzmin, Parolini, Burman, Ganesan, Tobiska [49] at $t = 3$ s.

[49], compared to the bubble shape predicted by the standard method.

6. Conclusion

HLLC Riemann solver was equipped with a conservative preconditioning technique to simulate two-phase flows with different degrees of flow compressibility. Furthermore, THINC interface sharpening method was applied to enhance interface capturing capability of the flow solver. Several test cases including air-helium shock-tube problem, shock cavity interaction, underwater explosion, and Rayleigh-Taylor instability, were used to examine the performance of the numerical methodology. Thus the flow solver was applied to a variety of compressible multiphase flows with a diverse range of physical characteristics such as, shock-interface interaction, gravity driven flows, viscosity and surface tension. Compared to previous studies, the present results are closely in line with available numerical and experimental data.

Furthermore, two more benchmark problems with incompressible nature, namely broken dam and rising bubble were probed to assess the performance of the employed preconditioning technique. It can be concluded that using the preconditioning technique results in better consistency with data obtained by incompressible methodology. Moreover, the preconditioned system switches back to the standard system in high Mach number flow regions thus preserving the compressibility attributes of the flow field. In conclusion, the developed flow solver has proven to be a promising tool in simulating multiphase flows, with a variety of characteristics Mach numbers ranging from unity to near zero.

References

- [1] F. Salvador, J.-V. Romero, M.-D. Roselló, D. Jaramillo, Numerical simulation of primary atomization in diesel spray at low injection pressure, *Journal of Computational and Applied Mathematics*, 2015.
- [2] R. B. Medvitz, R. F. Kunz, D. A. Boger, J. W. Lindau, A. M. Yocum, L. L. Pauley, Performance analysis of cavitating flow in centrifugal pumps using multiphase CFD, *Journal of Fluids Engineering*, Vol. 124, No. 2, pp. 377-383, 2002.
- [3] R. Kolakaluri, S. Subramaniam, M. Panchagnula, Trends in multiphase modeling and simulation of sprays, *International Journal of Spray and Combustion Dynamics*, Vol. 6, No. 4, pp. 317-356, 2014.
- [4] A. Irannejad, F. Jaber, Numerical study of high speed evaporating sprays, *International Journal of Multiphase Flow*, Vol. 70, pp. 58-76, 2015.
- [5] S. Subramaniam, Lagrangian-Eulerian methods for multiphase flows, *Progress in Energy and Combustion Science*, Vol. 39, No. 2, pp. 215-245, 2013.
- [6] R. O. Fox, Large-eddy-simulation tools for multiphase flows, *Annual Review of Fluid Mechanics*, Vol. 44, pp. 47-76, 2012.
- [7] R. Saurel, O. Lemetayer, A multiphase model for compressible flows with interfaces, shocks, detonation waves and cavitation, *Journal of Fluid Mechanics*, Vol. 431, pp. 239-271, 2001.
- [8] S. O. Unverdi, G. Tryggvason, A front-tracking method for viscous, incompressible, multi-fluid flows, *Journal of computational physics*, Vol. 100, No. 1, pp. 25-37, 1992.
- [9] V. Coralic, T. Colonius, Finite-volume WENO scheme for viscous compressible multicomponent flows, *Journal of computational physics*, Vol. 274, pp. 95-121, 2014.
- [10] D. A. Drew, S. L. Passman, Theory of multicomponent fluids, volume 135 of Applied Mathematical Sciences, Springer-Verlag, New York, 1999.
- [11] D. A. Drew, *Mathematical modeling of two-phase flow*, DTIC Document, pp. 1982.
- [12] M. Baer, J. Nunziato, A two-phase mixture theory for the deflagration-to-detonation transition (DDT) in reactive granular materials, *International journal of multiphase flow*, Vol. 12, No. 6, pp. 861-889, 1986.
- [13] R. Saurel, R. Abgrall, A multiphase Godunov method for compressible multifluid and multiphase flows, *Journal of Computational Physics*, Vol. 150, No. 2, pp. 425-467, 1999.
- [14] S. Kuila, T. R. Sekhar, D. Zeidan, A Robust and accurate Riemann solver for a compressible two-phase flow model, *Applied Mathematics and Computation*, Vol. 265, pp. 681-695, 2015.
- [15] C.-T. Ha, W.-G. Park, C.-M. Jung, Numerical simulations of compressible flows using multi-fluid models, *International Journal of Multiphase Flow*, Vol. 74, pp. 5-18, 2015.
- [16] A. Murrone, H. Guillard, A five equation reduced model for compressible two phase flow problems, *Journal of Computational Physics*, Vol. 202, No. 2, pp. 664-698, 2005.
- [17] G. Perigaud, R. Saurel, A compressible flow model with capillary effects, *Journal of Computational Physics*, Vol. 209, No. 1, pp. 139-178, 2005.
- [18] F. Xiao, S. Li, C. Chen, Revisit to the THINC scheme: a simple algebraic VOF algorithm, *Journal of Computational Physics*, Vol. 230, No. 19, pp. 7086-7092, 2011.
- [19] K. So, X. Hu, N. Adams, Anti-diffusion interface sharpening technique for two-phase compressible flow simulations, *Journal of Computational Physics*, Vol. 231, No. 11, pp. 4304-4323, 2012.
- [20] A. Tiwari, J. B. Freund, C. Pantano, A diffuse interface model with immiscibility preservation, *Journal of computational physics*, Vol. 252, pp. 290-309, 2013.
- [21] R. K. Shukla, C. Pantano, J. B. Freund, An interface capturing method for the simulation of multi-phase compressible flows, *Journal of Computational Physics*, Vol. 229, No. 19, pp. 7411-7439, 2010.
- [22] H. Luo, J. D. Baum, R. Lohner, Extension of Harten-Lax-van Leer Scheme for Flows at All Speeds, *AIAA journal*, Vol. 43, No. 6, pp. 1160-1166, 2005.
- [23] Y. Rong, Y. Wei, A flux vector splitting scheme for low Mach number flows in preconditioning method, *Applied Mathematics and Computation*, Vol. 242, pp. 296-308, 2014.
- [24] E. Turkel, Preconditioning techniques in computational fluid dynamics, *Annual Review of Fluid Mechanics*, Vol. 31, No. 1, pp. 385-416, 1999.
- [25] E. Turkel, V. Vasta, R. Radespiel, *Preconditioning Methods for Low-Speed Flows*, DTIC Document, pp. 1996.
- [26] S. LeMartelot, B. Nkonga, R. Saurel, Liquid and liquid-gas flows at all speeds, *Journal of Computational Physics*, Vol. 255, pp. 53-82, 2013.
- [27] E. Turkel, Preconditioned methods for solving the incompressible and low speed compressible equations, *Journal of computational physics*, Vol. 72, No. 2, pp. 277-298, 1987.
- [28] X.-s. Li, C.-w. Gu, Mechanism and Improvement of the Harten-Lax-van Leer Scheme for All-Speed Flows, *arXiv preprint arXiv:1111.4885*, 2011.
- [29] A. Murrone, H. Guillard, Behavior of upwind scheme in the low Mach number limit: III. Preconditioned dissipation for a five equation two phase model, *Computers & Fluids*, Vol. 37, No. 10, pp. 1209-1224, 2008.
- [30] E. F. Toro, 2009, *Riemann solvers and numerical methods for fluid dynamics: a practical introduction*, Springer Science & Business Media,
- [31] A. Harten, P. D. Lax, B. v. Leer, On upstream differencing and Godunov-type schemes for hyperbolic conservation laws, *SIAM review*, Vol. 25, No. 1, pp. 35-61, 1983.

- [32] K.-M. Shyue, F. Xiao, An Eulerian interface sharpening algorithm for compressible two-phase flow: The algebraic THINC approach, *Journal of Computational Physics*, Vol. 268, pp. 326-354, 2014.
- [33] K.-M. Shyue, An efficient shock-capturing algorithm for compressible multicomponent problems, *Journal of Computational Physics*, Vol. 142, No. 1, pp. 208-242, 1998.
- [34] F. Harlow, A. Amsden, Fluid dynamics: A LASL monograph(Mathematical solutions for problems in fluid dynamics), 1971.
- [35] T. Flåtten, A. Morin, S. T. Munkejord, On solutions to equilibrium problems for systems of stiffened gases, *SIAM Journal on Applied Mathematics*, Vol. 71, No. 1, pp. 41-67, 2011.
- [36] B. van Leer, Towards the ultimate conservative difference scheme, *Journal of Computational Physics*, Vol. 135, No. 2, pp. 229-248, 1997.
- [37] J. Brackbill, D. B. Kothe, C. Zemach, A continuum method for modeling surface tension, *Journal of computational physics*, Vol. 100, No. 2, pp. 335-354, 1992.
- [38] N. T. Nguyen, M. Dumbser, A path-conservative finite volume scheme for compressible multi-phase flows with surface tension, *Applied Mathematics and Computation*, Vol. 271, pp. 959-978, 2015.
- [39] H. Terashima, G. Tryggvason, A front-tracking/ghost-fluid method for fluid interfaces in compressible flows, *Journal of Computational Physics*, Vol. 228, No. 11, pp. 4012-4037, 2009.
- [40] R. R. Nourgaliev, T.-N. Dinh, T. G. Theofanous, Adaptive characteristics-based matching for compressible multifluid dynamics, *Journal of Computational Physics*, Vol. 213, No. 2, pp. 500-529, 2006.
- [41] N. Bourne, J. Field, Bubble collapse and the initiation of explosion, in *Proceeding of, The Royal Society*, pp. 423-435.
- [42] S. Majidi, A. Afshari, A ghost fluid method for sharp interface simulations of compressible multiphase flows, *Journal of Mechanical Science and Technology*, Vol. 30, No. 4, pp. 1581-1593, 2016.
- [43] K.-M. Shyue, A wave-propagation based volume tracking method for compressible multicomponent flow in two space dimensions, *Journal of Computational Physics*, Vol. 215, No. 1, pp. 219-244, 2006.
- [44] X. Hu, N. Adams, G. Iaccarino, On the HLLC Riemann solver for interface interaction in compressible multi-fluid flow, *Journal of Computational Physics*, Vol. 228, No. 17, pp. 6572-6589, 2009.
- [45] J. W. Grove, R. Menikoff, Anomalous reflection of a shock wave at a fluid interface, *Journal of Fluid Mechanics*, Vol. 219, pp. 313-336, 1990.
- [46] D. E. Fyfe, E. S. Oran, M. Fritts, Surface tension and viscosity with Lagrangian hydrodynamics on a triangular mesh, *Journal of Computational Physics*, Vol. 76, No. 2, pp. 349-384, 1988.
- [47] J. Martin, W. Moyce, Part IV. An experimental study of the collapse of liquid columns on a rigid horizontal plane, *Philosophical Transactions of the Royal Society of London A: Mathematical, Physical and Engineering Sciences*, Vol. 244, No. 882, pp. 312-324, 1952.
- [48] H. Guillard, C. Viozat, On the behaviour of upwind schemes in the low Mach number limit, *Computers & fluids*, Vol. 28, No. 1, pp. 63-86, 1999.
- [49] S. Hysing, S. Turek, D. Kuzmin, N. Parolini, E. Burman, S. Ganesan, L. Tobiska, Quantitative benchmark computations of two-dimensional bubble dynamics, *International Journal for Numerical Methods in Fluids*, Vol. 60, No. 11, pp. 1259-1288, 2009.
- [50] R. Clift, J. R. Grace, M. E. Weber, 2005, *Bubbles, drops, and particles*, Courier Corporation,